Article



Dendritic cell force-migration coupling on aligned fiber networks

Christian Hernandez-Padilla, Ben Joosten, Alme Franco, Alessandra Cambi, Koen van den Dries, Alme Franco, Alessandra Cambi, Koen van den Dries, Alessandra Cambi, Koen van den Dries, Alessandra Cambi, Koen van den Dries, Alessandra Cambi, Ca

¹Department of Mechanical Engineering, Virginia Tech, Blacksburg, Virginia; ²Department of Medical BioSciences, Radboud University Medical Center, Nijmegen, the Netherlands; and ³Children's Hospital of Philadelphia, Philadelphia, Pennsylvania

ABSTRACT Dendritic cells (DCs) are antigen-presenting cells that reside in peripheral tissues and are responsible for initiating adaptive immune responses. As gatekeepers of the immune system, DCs need to continuously explore their surroundings, for which they can rapidly move through various types of connective tissue and basement membranes. DC motility has been extensively studied on flat 2D surfaces, yet the influences of a contextual 3D fibrous environment still need to be described. Using ECM-mimicking suspended fiber networks, we show how immature DCs (iDCs) engage in migratory cycles that allow them to transition from persistent migration to slow migratory states. For a subset of iDCs with high migratory potential, we report the organization of protrusions at the front of the cell body, which reverses upon treatment with inflammation agent PGE2. We identify an unusual migratory response to aligned fiber networks, whereby iDCs use filamentous protrusions to attach laterally and exert forces on fibers to migrate independent of fiber alignment. Increasing the fiber diameter from 200 to 500 nm does not significantly affect the migratory response; however, iDCs respond by forming denser actin bundles around larger diameters. Overall, the correlation between force-coupling and random migration of iDCs in aligned fibrous topography offers new insights into how iDCs might move in fibrous environments in vivo.

SIGNIFICANCE Dendritic cells (DCs) are immune cells that patrol our bodies in search of invaders. While doing so, they encounter tissue microenvironments with different mechanical and topographical properties due to extracellular matrix (ECM) composition and organization. These properties are known to influence the function of many cell types including fibroblasts and stem cells but much less is known about their effect on immune cells. Using our ECM-mimicking nanofiber platform with precise control over fiber spacing and diameter and the ability to measure forces, we present new knowledge on DC adhesion and migration strategies. Our study increases our understanding of ECM-immune cell interactions that are important for pathophysiological processes such as wound healing, infection, cancer, and response to implants.

INTRODUCTION

Dendritic cells (DCs) are specialized cells of the immune system that bridge innate and adaptive immunity. They emerge from the hematopoietic system (1), where common myeloid progenitors differentiate into the pre-DC population that resides in the blood, lymphoid, and peripheral tissues as immature DCs (iDCs) (2). In peripheral tissues, iDCs adopt a slow migratory phenotype while patrolling for pathogenic antigens (3). After antigen uptake, iDCs differentiate into mature DCs (mDCs), switch to a fast migratory phenotype, and migrate to lymph nodes (4). In

Submitted August 21, 2023, and accepted for publication July 8, 2024.

Editor: Deborah Leckband.

https://doi.org/10.1016/j.bpj.2024.07.011

© 2024 Biophysical Society. Published by Elsevier Inc.

All rights are reserved, including those for text and data mining, AI training, and similar technologies.

lymph nodes, mDCs activate T cells, resulting in an antigen-specific immune response. The migratory switch during DC maturation is regulated by changes in the organization of the cytoskeleton induced by prostaglandin E₂ (PGE2). PGE2 contributes to inflammation and can enhance the infiltration of immune cells into various tissues by increasing vascular permeability (5). Specifically, in iDCs, PGE2 induces the dissolution of adhesive actin-based structures called podosomes, which are essential for the fast migration of mDCs (6–9).

To perform their immune function, iDCs must migrate through various extracellular matrix (ECM) environments such as connective tissue and basement membranes (10–12). In vivo, iDCs move by generating contractile forces in the fibrous ECM and by squeezing between small spaces (13,14). Interestingly, it has been shown that iDCs



*Correspondence: Koen.vandenDries@radboudumc.nl or nain@vt.edu

adopt an ameboid phenotype in porous 3D gels, while they use a mesenchymal migration mode in dense 3D environments exploiting podosomes to adhere to and degrade the matrix (8). iDCs are further known to migrate by exerting low traction forces around the migrating cell body (15). While iDC traction forces on various platforms are well established, contractile forces in a fibrous medium, such as implantable biomaterials, are not well known. Knowledge of iDC interaction with fibrous materials can be important considering the adjuvant effects of DC-mediated immunity on implantable 3D biomaterial gels (16). iDCs are among the first cells to interact with implants after proteins like fibronectin, vitronectin, or albumin deposit on the surface to promote cell adhesion (17). Furthermore, the material properties of foreign bodies including shape, stiffness, roughness, and nanofiber porosity have been linked to stronger/weaker inflammatory responses (18,19). A vast majority of studies on adaptive immune responses have focused on macrophages, while the interactions of iDCs with such fibrous implants remain understudied (16,20). Studies that mimic the fibrous conditions of the ECM can therefore provide valuable insight that broadens our understanding of iDC migratory and immune surveillance mechanisms.

Previous iDC migratory studies in 3D fibrous collagen lattices have shown how the deformation of polymerized gels results in regions of fiber alignment that can increase directional persistence in iDC migration (21). Furthermore, substrate topographical cues have been shown to prevent PGE2-mediated RhoA activation resulting in faster podosome dissolution rates (22). While studies on microfabricated anisotropic architectures reported increases in iDC speed and persistence influenced by the alignment of confined spaces (23), other studies using microchannels with iDCs have shown migration modes characterized by cycles of rapid migration/high motility and arrest/low motility, which was absent on flat substrates (24,25). Overall, it has been established that iDCs are sensitive to shape, alignment, and the confinement offered by the 3D properties of their surroundings, and the mechanotransductive role of the ECM topography remains an active area of study for iDCs (26,27). While traction forces using micropillars have been linked to the migratory direction with iDC filopodial or dendritic extensions (28), few studies have investigated iDC migration in the context of fiber-based methods, and none explored the role of forces in fiber networks for iDC migration.

Cell migration on 2D flat coverslips and 3D fibrous environments is known to be very different due to the changes in cell morphology and migratory modes (29–33). To capture the interactions of fiber architecture on cell migration, we used fiber networks fabricated using our previously reported nonelectrospinning spinneret-based tunable engineered parameters (STEP) technique (34,35). We sought to describe iDC migratory responses to fibers as those occurring in vivo or on implantable fibrous materials. We chose aligned fibers

as cells usually migrate persistently along the fiber axis (36,37), which provides a straightforward template to interrogate cell behavior on fibers. Furthermore, we used Nanonet force microscopy to quantify iDC contractility (38–42). We discovered that, while a large portion of iDCs were in a nonmotile state, a subset of the population used their filamentous protrusions to attach laterally and tug on neighboring fibers to migrate independently of fiber alignment and density. Interestingly, we found that iDCs switched the concentration of their protrusions from front to rear in the presence of PGE2. Increasing the fiber diameter resulted in denser actin networks but did not affect the migratory behavior. Overall, we present new knowledge in immune cell mechanobiology by interrogating the topological interactions and force-driven migration of iDCs in ECMmimicking fiber networks.

MATERIALS AND METHODS

Scaffold preparation

Using our previously developed nonelectrospinning STEP technique (34,35,43), suspended fiber nanonets composed of 200 or 500 nm diameter fibers spaced 12 μ m apart were deposited orthogonally on 2 μ m diameter fibers spaced 300 μ m apart. Nanofibers for 200 and 500 nm were manufactured from solutions of polystyrene (MW = $2,500,000 \text{ g mol}^{-1}$; cat. no. 1025; Scientific Polymer Products, Ontario, NY) dissolved in xylene (X5-500; Thermo Fisher Scientific, Waltham, MA) in 6 and 9 wt % solutions. Fiber diameters were chosen to match the diameters of individual collagen fibrils (44). Two-micrometer diameter fibers were manufactured from 5 wt % of high-molecular-weight polystyrene (MW = 15,000,000 g mol⁻¹, Agilent Technologies, Santa Clara, CA). The polymeric solutions were extruded through micropipettes with an inside diameter of 100 µm (Jensen Global, Santa Barbara, CA) for the deposition of fibers on a hollow substrate. All fiber networks were cross-linked at intersection points using a custom fusing chamber, to create fixed-fixed boundary conditions (interface of small and large diameter fibers).

Cell culturing and drug inhibition experiments

iDCs were generated from peripheral blood mononuclear cells (PBMCs) (45,46). Monocytes were derived either from buffy coats or from a leukapheresis product, purchased at Sanquin Blood Bank, Nijmegen, the Netherlands. PBMCs were isolated by Ficoll density gradient centrifugation (GE Healthcare Biosciences, Piscataway, NJ, 30 min, 4°C, 2100 rpm). PBMCs were extensively washed in cold phosphate-buffered saline (PBS) supplemented with 0.1% (w/v) bovine serum albumin (BSA) (Roche Diagnostics, Indianapolis, IN) and 0.45% (w/v) sodium citrate (Sigma-Aldrich, St. Louis, MO). PBMCs were seeded in plastic culture flasks and left to adhere for 1 h in Roswell Park Memorial Institute (RPMI) 1640 medium (Life Technologies, Carlsbad, CA) supplemented with 2% human serum. Next, cells were washed three times with PBS to remove the lymphocytes and nonadherent monocytic cells and isolate the monocytes by plastic adherence. The adherent monocytes were subsequently cultured in RPMI 1640 medium supplemented with 10% fetal bovine serum (FBS) (Greiner Bio-One, Frickenhausen, Germany), 1 mM ultraglutamine (BioWhittaker, Walkersville, MD), antibiotics (100 μ g mL⁻¹ penicillin, 100 μ g mL⁻¹ streptomycin, and $0.25 \,\mu g \, \text{mL}^{-1}$ amphotericin B, Gibco, Thermo Fisher Scientific) for 5 or 6 days, in a humidified, 5% CO₂-containing atmosphere. DC differentiation was induced by the addition of IL-4 (500 μ g mL⁻¹) and GM-CSF (800 μ g mL^{-1}) to the culture medium (45,46). On day 5 or 6, cells were collected, suspended in cryomedium (10% DMSO, 40% FBS, and 50% medium), and stored in cryovials in liquid nitrogen.

Cells were cultured on T75s using RPMI (Gibco, Thermo Fisher Scientific) with 10% FBS (Invitrogen, Carlsbad, CA). STEP-spun scaffolds were attached on six-well plates using corning vacuum grease (the experimental assembly of the scaffolds is depicted in Fig. S1), disinfected with 70% ethanol, and then coated with 4 μ g/mL of fibronectin (cat. no. FNR01, Cytoskeleton, Denver, CO) by incubating at 37°C for 1 h. DCs were lifted from T75s by incubating at 4°C with PBS; the resuspended cells were seeded onto STEP-spun scaffolds at low densities to avoid cell-cell interactions, allowed to attach for at least 2 h, and the wells were flooded with 3 mL of RPMI + 10% FBS. DCs for PGE2 stimulated studies were lifted after 8 h of stimulation while incubated at 37°C. Drug inhibition experiments were performed following the same culture protocol; blebbistatin $(20 \mu M)$, CK666 $(100 \mu M)$, and SMIFH2 $(20 \mu M)$ were added 2 h postseeding on the scaffolds.

Migration and protrusion analysis

Cells attached to nanofiber architectures were imaged at 5-min intervals for 8 h with an AxioObserver Z1 (Carl Zeiss, Jena, Germany) using a 20 × 0.8 NA objective. Experimental data were collected across at least three independent experimental rounds per category. The centroid of the cells was tracked by drawing the cell outlines, which were used to calculate the instantaneous velocities, angular displacements, persistence, and meansquared displacement (MSD). Migratory persistence (P) is defined as:

$$P = \frac{Net \, Displacement}{Contour \, Length} \tag{1}$$

MSDs are defined by the equation:

$$MSD(\tau) = \langle [x(t+\tau) - x(t)]^2 + [y(t+\tau) - y(t)]^2 \rangle$$
 (2)

$$MSD(t) = 2Dn_d \left(\Delta t - P \left(1 - e^{-\frac{\Delta t}{P}} \right) \right)$$
 (3)

$$MSD = 4D\Delta t^{\alpha} \tag{4}$$

where D is the diffusion coefficient, n_d is the dimensionality for the random-walk diffusion, and P is the persistence time. The database of CSV files from ImageJ manual measurements and tracking functions was loaded into R Studio for plotting and analyzing. The reported values for the diffusion coefficients and MSD exponents were selected only for those satisfying the model with $R^2 \ge 0.8$ where 80.8% of the cells analyzed satisfied this condition. Vectorial analysis of the protrusion positions of the migrating cell used the information manually measured in ImageJ from 40× bright-field videos imaged every 5 s for 15 min. From these vectors, as shown schematically in section "Filamentous lateral protrusions guide migration independent of underlying anisotropy", we calculated the scalar product of the vectors $(v_c \cdot v_p)$ and, by counting positive and negative results, we determined the directionality of the vectorial pairs. Protrusive events were classified as front or back if they had 50% of their time points in one direction or the other.

Statistics and determining speed subsets

The data set was tested for statistical significance using Tukey's honestly significant difference for multiple comparisons between overall categories and subcategories (p values: *p = 0.05, **p = 0.01, ***p = 0.001). Population velocity was positively skewed with a value of 4.98 (Fig. S2 A). Furthermore, the qqplot showed that the theoretical quantiles began to deviate into outliers for speeds higher than 0.25 $\frac{\mu m}{min}$ (Fig. S2 B). Once the domain was kept at $0 < speed < 0.25 \frac{\mu m}{min}$ data followed a normal distribution (Fig. S2 C) and had a skewness value of 0.51 for the low migratory subset population. Data followed normal distributions through normality tests and theoretical quantile plots. Fig. S2 D shows qualitatively low deviation tails (skewness value of 0.95), thus justifying key assumptions to use Tukey's honestly significant difference method for the multiple comparisons in the paper. Data used for comparison plots were subset using the mentioned $0.25 \mu m/min$ cutoff, and cells with these speed characteristics had distinct migratory patterns. All significant comparison tests reported were for this subpopulation of DCs. Finally, the significance of the changes in protrusion proportions was calculated from Eq. 5 for two independent samples with dichotomous outcomes (front and back).

$$z = \frac{\hat{p}_1 - \hat{p}_2}{\sqrt{\hat{p}(1-\hat{p})\left(\frac{1}{n_1} - \frac{1}{n_2}\right)}}$$
 (5)

Force studies

Migratory cases were randomly selected for the force calculations. Forces were calculated through a custom-built MATLAB pipeline that ran an optimization algorithm to match the tracked fiber deflections with computational finite-element fiber deflections (42,47). Forces only report vertical force components representing filamentous interactions with the fibers that can be considered to be point loads. Using the aforementioned fiber networks, the Nanonet force microscopy resolution is ± 2 nN, therefore forces below 2.0 nN were considered as noise and reported as NA values (48). Front and back categories of forces were determined from the net migration direction of the path and the position of the cell centroid to the fibers. Side forces represent instances when the analyzed cell stops, and migrates to the

Immunofluorescence and imaging

iDCs were fixed with 4% paraformaldehyde, permeabilized with 0.1% Triton X-100 solution, and blocked with 5% goat serum. F-actin was stained using rhodamine phalloidin (Santa Cruz Biotechnologies) at a ratio of 1:100 of an antibody dilution buffer with 1% BSA in PBS. DAPI stock solution was diluted with a ratio of 1:80 of the buffer. Vinculin (hVin-1) primary antibody (Sigma-Aldrich) staining images were diluted with a ratio of 1:200 and conjugated with Alexa Fluor 488 (Invitrogen) secondary antibodies. Fixed samples were imaged on an LSM 880 (Carl Zeiss) using a 63× 1.2 NA water immersion objective. Multiple immunofluorescent rounds reused imaging settings defined in the first experiment for crosssample comparisons. Laser power across multiple samples was 0.2% for 405 nm and 4% for 543 nm. Fluorescent images and actin heatmaps were postprocessed and rendered in Zen blue (Zeiss) using look-up tables to show the differences in fluorescent intensity.

RESULTS

DC shapes and speed on suspended aligned fiber networks

To assess the behavior of iDCs on suspended fiber networks, we deposited aligned fibers of 200 and 500 nm diameters with an interfiber spacing of 12 μ m (Fig. 1 A) so that cells could attach to at least two fibers. Unexpectedly, iDC shapes had strikingly different responses to our previous studies of cells on fibers (41,49). We observed that, on both fiber

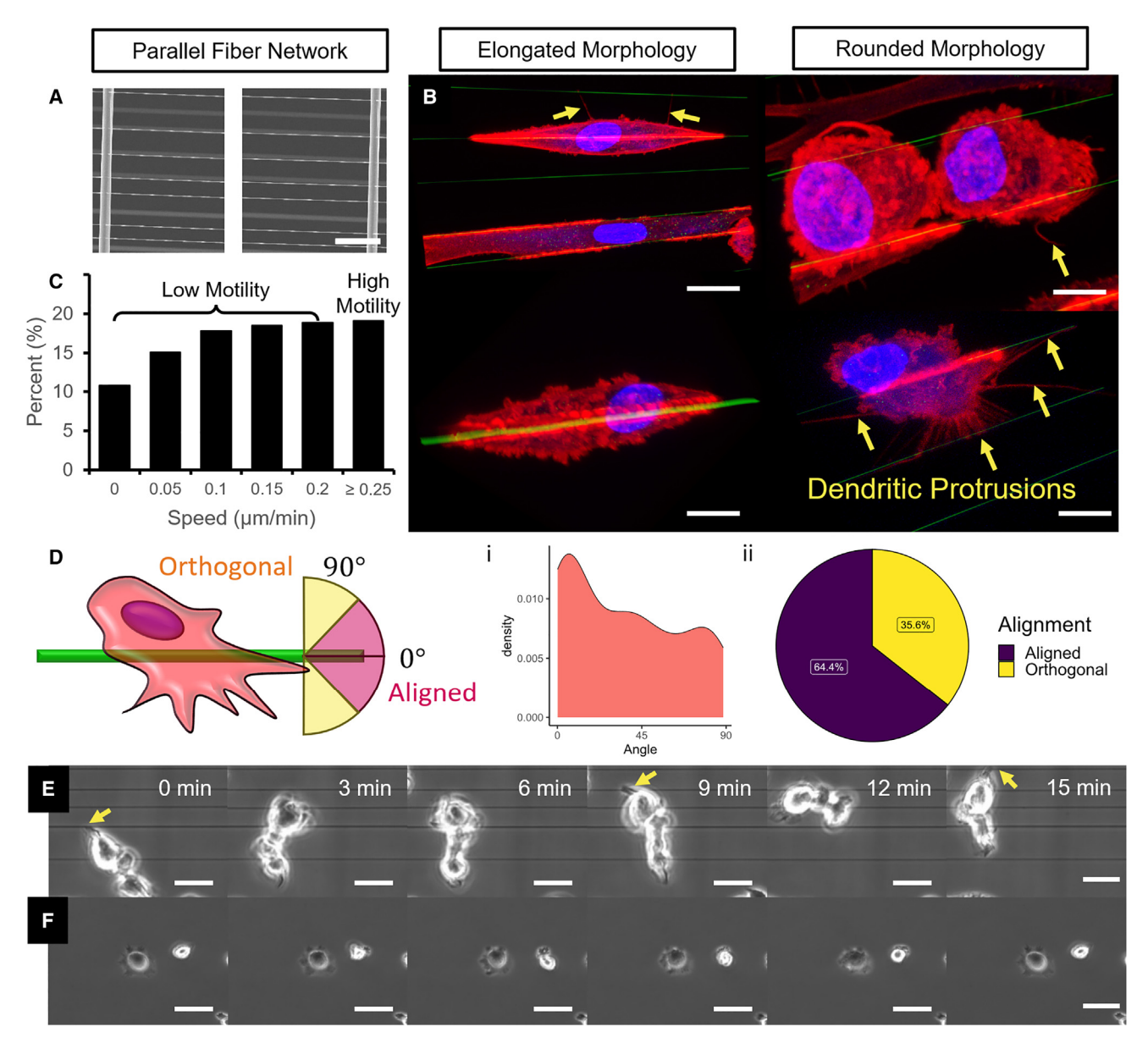


FIGURE 1 iDC shape and overall motility on nanonets. (A) SEM images of nanonets composed of vertical base fiber posts (\sim 2000 nm diameter) and orthogonally aligned 200 nm fibers. (B) Confocal images of iDCs stained for actin with rhodamine-phalloidin (red), a nucleus with DAPI (blue), and suspended fibers (green). Cells either elongated along the fiber axis or remained rounded on fiber networks. Filamentous protrusions are pointed by yellow arrows. (C) Histogram of DC migration shows that \sim 80% of the population exists in a nonmotile phenotype (elongated morphologies); however, \sim 20% (rounded morphologies) migrate at speeds greater than or equal to 0.25 μ m/min (n = 98). Migratory data were collected over 2 h. (D) The cell body orientation was determined from ImageJ analysis and binned into aligned and orthogonal groups as depicted in the schematic. (i) Density plot that shows the distribution of cell body orientations for iDC (n = 74). (ii) Pie chart showing percentages of alignment using the binning described in the schematic. (E) Time-lapse images illustrating the migratory behavior of iDCs in fibronectin-coated 500 nm aligned fibers with arrows pointing to filamentous protrusions as they occur throughout migration, and (F) on flat 2D control. Imaging was conducted at 3 min intervals. Scale bars, 10 μ m.

diameter categories, a portion of iDCs sensed fibers by adopting elongated shapes along the fibers, while another portion remained oblong, with some cases boasting dynamic filamentous structures (Fig. 1 B). We proceeded to investigate the distribution of iDC alignment and migration speed on fibers (Fig. 1, C and D) to determine if we could establish a link between migration and this surprising response aligned fibers. We found that iDC body orientations were

uniformly distributed (from 0 to 90° , Fig. 1 D(i)), while other cell lines such as 3T3s (50), C2C12s (41), mesenchymal stem cells (48), and U251s (37) are well established to respond in favor of horizontal alignment (closer to 0°). Approximately 95% of other cells become aligned to the fibers as opposed to 63% for iDCs (Fig. 1 D(ii)). This revealed that iDCs had a subpopulation (37%) of cells that were independent of the alignment of the fibers, which we

believed could be linked to different migration modes. The distribution of average migration speeds (Fig. S2 A) did not match the uniform distribution of the body alignments. We found that approximately 80% of iDCs on fibers, migrated at speeds lower than 0.25 μ m/min (Fig. 1 C). Furthermore, this speed was an important separation point for the tails in the data, where all of the subsequent points above this mark, began to separate from the theoretical trend for a normal distribution (skewness of 4.98, Fig. S2 B). We separated the data for the nonmigratory population (Fig. S2 C) and this lowered the skewness to 0.51, suggesting that the nonmigratory cells followed a normal distribution. The migratory subset which represented 20% of the population (Fig. 1 C) also followed a normal distribution (Fig. S2 D) with a skewness of 0.95. This revealed that the majority of the cells were predisposed to low motility, a behavior expected of iDCs, while around 20% were found to be fast moving (>0.25 μ m/min) (Figs. 1 C and S2, A and B), a behavior unique to the population on the fibers. In comparison, on flat 2D substrates, the iDC population exhibited significantly $(p_{adi} = 2.26 \times 10^{-6})$ slower migration speeds on average $(0.13 \pm 0.13 \mu \text{m/min}, \text{Fig. S3})$ to those on fibers. These initial findings exposed that fibers significantly enhanced iDC motility and that the fiber population was split into previously unknown nonmigratory and migratory subpopulations of iDCs.

The migration speeds revealed that to analyze iDC migration we must focus on a subset of the population. We hypothesized that iDC shapes could help us predict these migratory functions on the fibers. iDCs on fibers had pseudopod-like structures while the main cell body remained in oblong shapes of varied circularities (Fig. 1, B) and E), suggesting that shape indexes such as circularity could predict the cell's migratory state. In contrast, on flat substrates cells were consistently in spread shapes with large pseudopods (Figs. 1 F and S3). The visible differences between morphology fibers and flat substrates also reinforced that morphological differences could correlate with migratory states. We quantified cell shapes in migration and found an unexpectedly large variability for areas, circularities, and aspect ratios of migratory (Fig. S4) and nonmigratory (Fig. S5) cells. DC projected areas on fibers ranged between 600 and 1200 μm^2 and circularities between 0.09 and 0.9. We used the standard deviation of the bright-field video stacks in ImageJ (Fig. S6 B) to qualitatively show the differences in hotspots, representing regions of slower migration with dynamic changes of DC shapes. We plotted these shape fluctuations (Fig. S6, A-D) and attempted to find a correlation between circularity and speed (Fig. S6 E), which to our surprise revealed a nearly uniform distribution of circularities and speeds. Thus, we concluded that iDC shapes were so dynamic on fibers that it made it troublesome to implement any reliable shape segmentation approach. We proceeded to only consider cells that on average migrated faster than the 0.25 µm/min threshold. Overall, compared with flat 2D substrates, suspended fiber architecture produced a heterogeneity in iDC shapes and revealed a subpopulation of cells that roamed over the scaffold at high speeds.

PGE2 stimulation enhances migratory persistence without affecting speed

iDC migration and adhesion on various substrates are controlled by many of the same proteins as focal adhesions, including vinculin (51). Cell adhesion is an essential structure in effective migration; thus, to understand the cytoskeletal differences of iDCs and their podosomes across substrates, we used immunofluorescence of actin and vinculin. For both cells on fibers and flat 2D substrates, we observed diffusive actin cytoskeletons (Figs. 1 B and S3), which correlates to iDC's capacity to adopt highly dynamic shapes. Notably, cells had regions of actin enrichment at the locations of the fibers (Fig. 1 B), whereas in flat 2D substrates they had ring-like structures (Fig. S3). Vinculin staining confirmed that these enrichment regions were podosomes on the fibers and in flat 2D substrates (Figs. 2, S7, and S8). On fibers (Fig. 1 B), not all cells had regions of enrichment or podosomes, in

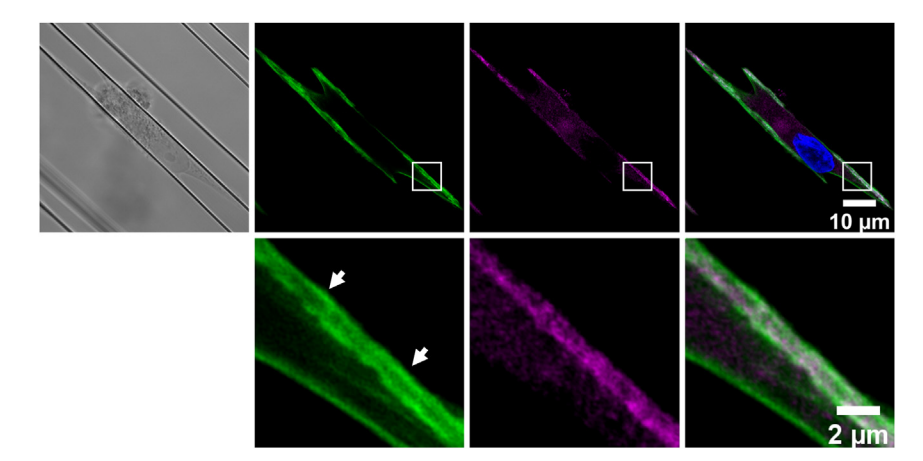


FIGURE 2 iDCs form podosome-like structures along the fibers. Representative confocal microscopy image of a iDC immunostained with actin (green) and vinculin (magenta) and the nucleus (blue). The enlargement shows the typical central localization of actin surrounded by vinculin.

correlation with the overarching subpopulations determined by speed. This suggested that new DC migration phenotypes on fibers could be driven by the dissolution of podosomes; a parallel to established research in flat 2D substrates (22). We had reasonable suspicion that perturbing iDC podosome adhesion with PGE2 and varying fiber diameters could be important drivers of these new iDC subpopulations.

When we manually tracked iDCs, we expected them to sense the fiber alignment and result in 1D persistent migration. Yet, we found that this fast-moving subpopulation of cells engaged in random walks even in the presence of the contact guidance of our highly aligned fiber networks (Fig. 3 A) and notably shown by their migration turning angles (Fig. S9). We found this to be strikingly different from our previous studies on the role of substrate alignment (37,48,52,53). We stimulated iDCs in culture with PGE2 and anticipated an increase in migration speed as well as persistence (7). We found that PGE2-stimulated iDCs traveled significantly ($p_{adj} = 0.034$) more persistent on 200 nm fibers; however, this effect was not shared with the 500 nm fibers (Fig. 3 B). PGE2 caused a nonstatistically significant ~25% mean increase in migratory persistence on 500 nm fibers ($Pers_{Control} = 0.24 \pm 0.15$; $Pers_{PGE2} =$ 0.31 ± 0.20), whereas on 200 nm fibers it caused a significant \sim 66% mean increase ($Pers_{Control} = 0.16 \pm 0.13$; $Pers_{PGE2} = 0.32 \pm 0.19$ for 200 nm fibers, Fig. 3 B). Contrary to what we expected, we found that iDC average speeds on fiber networks remained largely unchanged after PGE2 stimulation ($S_{control} = 1.59 \pm 0.66 \frac{\mu m}{min}$; $S_{PGE2} =$ $1.65 \pm 0.86 \frac{\mu m}{min}$ for 500 nm fibers and $S_{Control} = 1.63 \pm$ $1.86 \frac{\mu m}{min}; S_{PGE2} = 1.34 \pm 0.65 \frac{\mu m}{min}$ for 200 nm fibers Fig. 3 B). This contrasted the 0.4 μ m/min mean increase in flat 2D substrates after PGE2 stimulation (Fig. S3). Another characteristic we identified in this migratory subpopulation, is how they transitioned between higher and lower motility states (Fig. S10), as reflected by their changes in persistence and speed with time (Videos S1, S2, S3, S4, and S5). iDCs in 200 nm control cases had the largest ranges with instantaneous speeds ranging between 2 and 20 μ m/min; conversely, other categories ranged between 1 and 3 µm/min. We suspected that this drastic difference in speed fluctuations for iDCs on 200 nm fibers was largely driven by the changes in the available surface area of the smaller diameter. This result motivated us to consider the changes in cellular forces that we explore in further sections. Our analysis revealed enhanced migratory patterns on 200 nm fibers, whereas increasing the diameter or exposing the PGE2 enhanced the persistence of the migration, thus linking fiber size to iDC migration patterns.

We proceeded with time-independent comparisons by looking at MSD curves. MSD profiles were fitted to Eq. 4 (see materials and methods) where an $\alpha < 1$ represents depressed motion, $\alpha = 1$ describes a random walk, and $\alpha > 1$ is reflective of more directional motion. For both fiber

diameters, we reported nonstatistically significant shifts in the mean for α -scaling exponents; however, for 200 nm fibers the ~26% change between control and PGE2 had a $p_{adj}=0.070$ (Fig. 3 C) ($\alpha_{control}=0.95\pm0.39$; $\alpha_{PGE2}=1.23\pm0.40$), which had a close agreement with our reported change in persistence for the same categories. iDCs for control/PGE2 and 200/500 nm fibers could patrol over large distances independent of the alignment of the underlying architecture, opposite to our expectations from previous studies using similar fiber architectures (53).

Lastly, we report that iDCs migrated significantly differently on fibers from 2D substrates for almost all migration metrics (Table 1). Cells migrating on the fibers had high protrusive activity in both motile and nonmotile populations in our migration videos (Videos S2, S3, S4, S4, and S5), which contrasted with their slower-moving pseudopods on flat 2D substrates (Video S1). Suspecting that protrusions mechanically drove cells to achieve higher speeds and the new phenotypes, we sought to test the role of actin branching, nucleators, and myosin in regulating iDC migration. The inhibition of formins (by SMIFH2) and myosin IIA (by blebbistatin) significantly impacted the migration of iDCs on fibers (Fig. S11), resulting in practically no discernible migration. The complete arrest of migration on fibers showed that actin nucleators (formins) and contractility (myosin IIA) were still retained as essential migratory mechanisms. However, when the Arp2/3 complex was pharmacologically inhibited (54), iDCs were still able to migrate slowly $(0.067 \pm 0.06 \frac{\mu m}{min})$, showing that actin branching facilitates migration but it is not essential. Our findings are similar to previous literature that suggested that Arp2/3 facilitated the forward locomotion of iDCs (55). Overall, we identified that the migratory behavior of iDCs had dynamic fluctuations, was influenced by fiber diameter, and had critical links to the protrusive/contractile ability of the cells.

Filamentous lateral protrusions guide migration independent of underlying anisotropy

Actomyosin-based contraction is essential for DC migration and antigen capture (56–58); therefore we aimed to characterize the force generation ability of iDCs on the suspended nanofibers. We were interested in determining if the random migration of iDCs on aligned fibers was influenced by force magnitudes and the orientation of these forces. It has been shown that DCs under the influence of shear stress in a microfluidic device exert higher forces and move persistently (59). Furthermore, the rearrangement of the cytoskeleton is well established to generate locomotion forces known to coordinate DC functions such as antigen processing, inflammatory cytokine production, and chemotactic migration (60). With this motivation in mind, we began a morphological analysis of iDC migration (imaged at 5 s intervals) where we manually

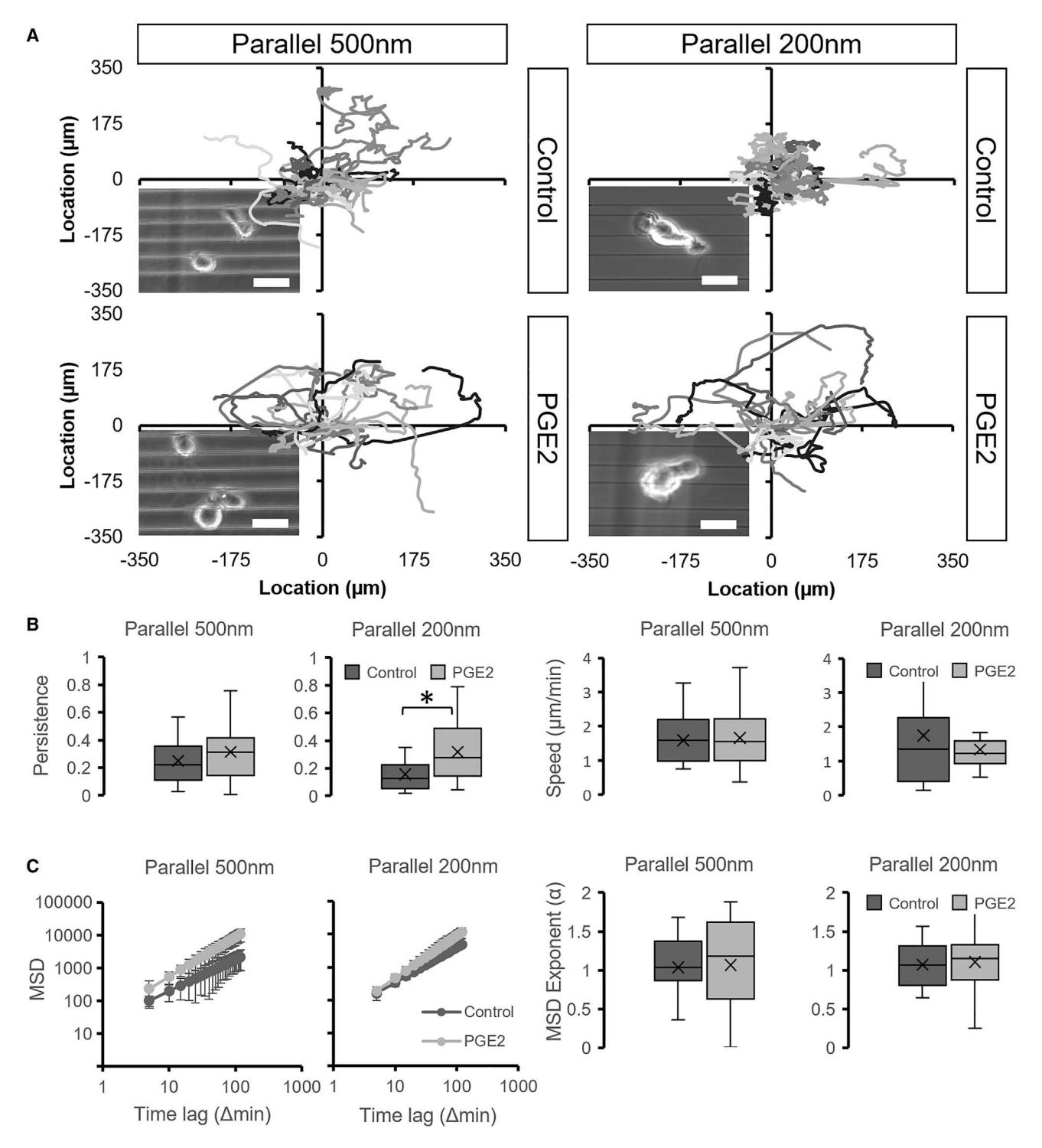


FIGURE 3 Effects of PGE2 on iDC migration along aligned fibers. (A) 2D scatter/line plot showing the difference in migratory paths along with corresponding optical images with and without PGE2 stimulation for the two fiber diameters. The total migration time for all groups is equal to 2 h. Scale bar, $20 \mu m$. (B) Persistence and migratory speeds for iDCs under PGE2 stimulation for the tested diameters. For parallel 200 nm the * $p_{adj} = 0.034$. (C) Experimental MSD plots organized by diameter subcategories (sample size of control-PGE2: 23–27 for 500 nm and 23–21 for 200 nm). Solid lines represent the average MSD profile experimentally calculated and the MSD exponent computed from MSD profiles. All boxplots without stars are NS p value comparisons that have been omitted.

segmented cells into three parts: the overall cell body (Fig. 4 A(i,ii); Videos S6, S7, S8, and S9), the body (minus the protrusions), and protrusions (Fig. 4 A(iii)).

We obtained the shape descriptors of the overall cell, the body, and the protrusions, thus allowing us to vectorially correlate iDC protrusive activity with migration

TABLE 1 p values for comparison between 2D and diameters

p values 2D vs. fibers			
Metric	Comparison	p_{adj}	Star
Speed	2D - 200 nm	1.93e-5	***
Speed	2D - 500 nm	2.26e-6	***
Persistence	2D - 200 nm	0.118	NS
Persistence	2D - 500 nm	8.38e-4	***
α	2D - 200 nm	1.12e-5	***
α	2D - 500 nm	2.62e-6	***

(Fig. 4 *B*). The analyzed cellular paths for all categories (Fig. 4 *C*) contained between 18 and 25 recorded protrusion events over 15 min. First, we looked at the locations of these protrusive events with respect to the cell centroid in 2D histograms and found that the position of iDC protrusions was also independent of fiber diameter (200/500 nm) and PGE2 stimulation (Fig. S12). However, the dot products of the protrusion vectors ($\overline{v_p}$ in Fig. 4 *B*) with respect to the migratory direction ($\overline{v_b}$ in Fig. 4 *B*) revealed that, on 200 nm fibers, 60% of protrusions formed at the front of the migrating body (42 front, 28 back, Fig. 4 *C*). This strikingly contrasted the PGE2 experimental group, where 71% the protrusions oriented toward the rear of the migrating body, a highly significant shift in

proportion ($p_{adj}=0.004$) (13 front, 32 back, Fig. 4 C). On the 500 nm diameter fiber networks, the effect on the differences in protrusive activity was reduced with nonsignificant proportions between populations (control: 33 front and 27 back; PGE2 stimulation: 10 front and 12 back, Fig. 4 C). Unfortunately, this analysis could not be extended to flat substrates as cells were observed to have broad lamellipodia instead of the filamentous protrusions we analyzed on fibers (Figs. S3 and S8). Our data suggest that iDCs migrate on fibers by concentrating active protrusive fronts that correlate with their direction of migration.

Forces on fibers concentrate behind and laterally to the direction of migration

We next sought to link cell migration and protrusive events with force vectors as the cell migrated. First, we observed that the low motile (elongated) cells attached to two fibers contracted the fibers inwards, signifying force exertions (Fig. 5 A). We characterized contractile forces of nonmotile iDCs attached to two 200 nm diameter fibers (Fig. 5 B(i)) with and without stimulation of PGE2. We found the contractile forces to slightly decrease with PGE2 stimulation

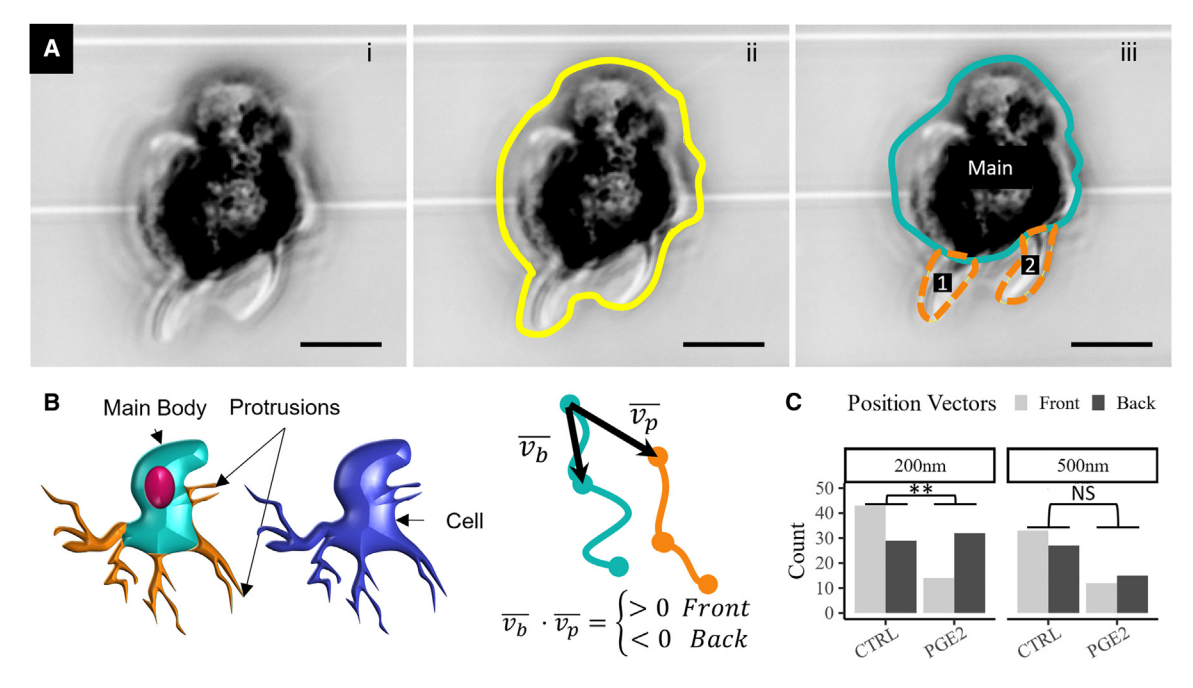


FIGURE 4 Vectorial correlation of DC protrusive activity with migration on aligned fibers. (A) Bright-field images showing an example cell and how the dynamic shapes of iDCs were manually segmented for dot product analysis of the iDCs. Scale bars, 5 μ m. (i) Reference image shown without annotation using the inverted lookup table (LUT). (ii) Representative depiction of gross cell body outlines. (iii) Manual segmentation of main body (Main) and protrusion sections (1 and 2) in teal (solid) and orange (dashed), respectively. (B) Schematic representation of main body and protrusion segmentation in teal and orange. The vector traces show the temporal approach for analyzing the directionality of the position of the protrusion with respect to the migrating body through the dot product of the vectors v_b (migration vector of the main body drawn from the current time "n" to the next time "n+1") to v_p (protrusion vector drawn from the current position of the body to the current position of the protrusion at time "n"). The path schematic shows the drawn vectors for mapping the position of the protrusions. The dot product of these vectors was used to ascertain if protrusions were at the front or back. (C) Protrusion counts with 50% or more incidence of front or back time points are counted for n=3 cells per diameter and drug category. Statistics were calculated with population proportions test using Eq. 5; for 200 nm $p_{adj} = 0.004$.

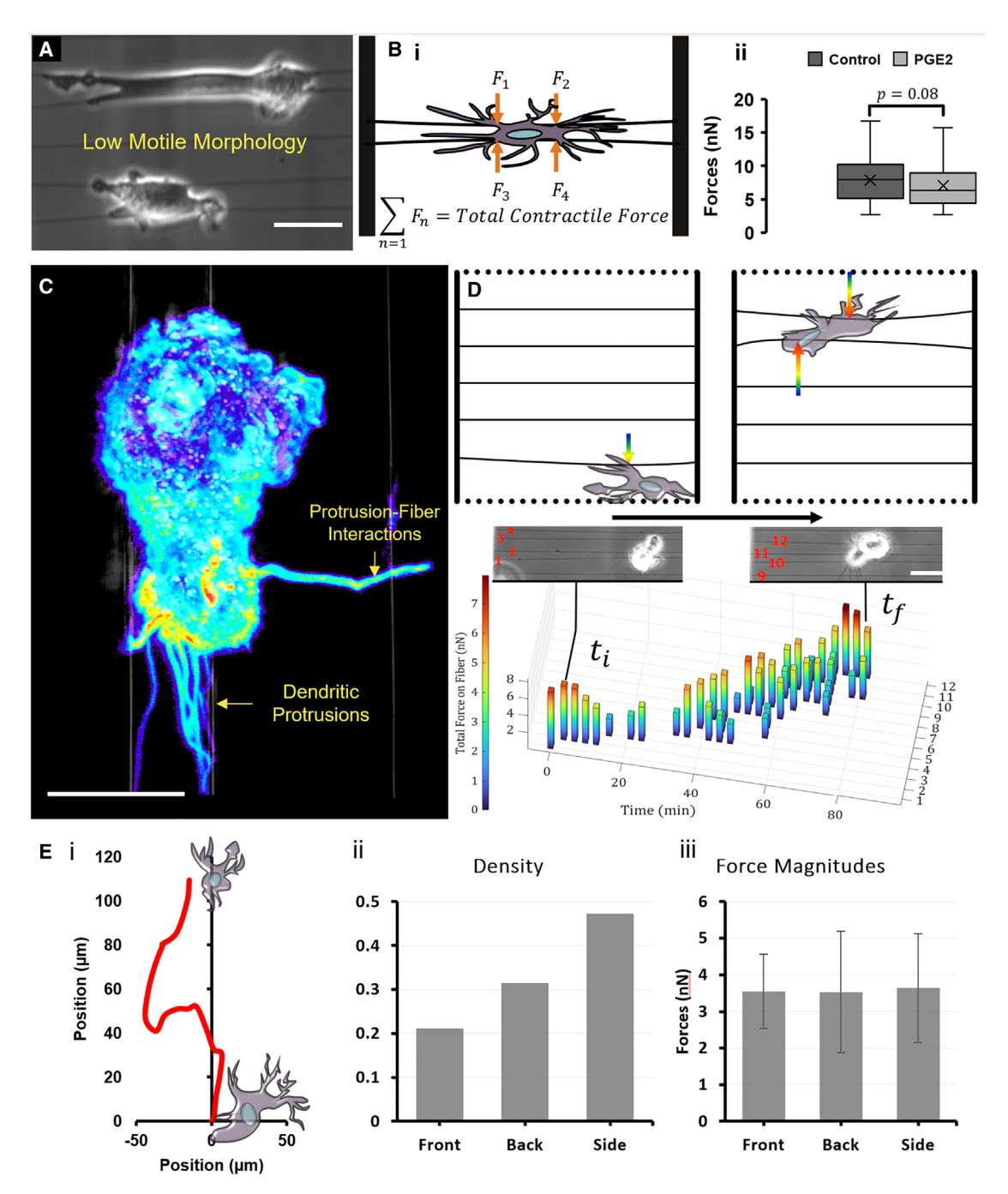


FIGURE 5 Analysis of contractile forces of DCs and their orientation in migration. (A) Bright-phase image illustrating the low motile morphologies used for the total contractile forces. Scale bar, $20 \ \mu m$. (B) (i) Illustration representing iDC low motile categories for total contractile forces added from 4 force vectors. (ii) Total contractile force between control and PGE2 groups on 200 nm fibers ($p_{adj} = 0.08$). (C) Immunostained iDC shown through actin heatmap LUT with annotations pointing to their filamentous protrusions. (D) Schematic depicting the perpendicular traction force vectors for the initial and final time points of the selected case with a 3D bar plot below representing the transient traction force exertion in a supplementary movie (Videos S6). Image insets at the top have the fiber number labels. Scale bar, $20 \ \mu m$. These two images correspond to the initial time (0 min) and final time (80 min). (E) (i) Example migration path of iDC with a straight segment of migration. (ii) Forces occurring in front, rear, and side that were plotted with respect to the cell centroid in migration. (iii) Respective force magnitudes show that the cell does not have a contractile bias for either configuration or location of the forces. For both bar plots, N = 4 migrating cells and n = 300 recorded forces at different time points.

($F_{ctrl}=7.3\pm3.36$ nN, $F_{PGE2}=5.9\pm3.73$ nN, Fig. 5 B(ii)). As in earlier sections, we wanted to compare with forces on 500 nm; however, the small deflections were not

easily measurable, thus not allowing us to estimate the forces. Morphologically, we compared actin clustering by immunofluorescence and found denser actin regions present

on 500 nm fibers (Fig. S13). In contrast to nonmotile cells, fast-moving cells had filamentous protrusions extending in alignment and laterally from the main cell body, thus being able to attach to the neighboring fibers (Figs. 5 *C*, S12, and S13). Having found slight contractile differences with PGE2 stimulation, and morphological differences in actin, next we focused on the lateral force interaction.

Knowing that protrusive activity concentrated at the front of the cell, we investigated if the concentration of forces coincided with the protrusive fronts of the migrating cell (Videos S10, S11, and S12). To obtain migration forces of iDCs, we analyzed cells with a persistent migration segment that spanned multiple force fibers (Fig. 5 D shown for a representative case). We recorded the forces as the iDC tugged on the fibers (Video S6) and found that the forces cycled from high (~9 nN) to low values (below 2 nN) as the cell migrated (Figs. 5 D and S14 A). Having cells interact with multiple aligned fibers allowed us to track the deflection of individual fibers as cell migration progressed, thus enabling us to investigate the occurrence of these forces relative to the cell centroid and the direction of migration (Fig. 5 E(i)). Tracking cell forces across the cell body revealed a higher incidence of forces behind the cell centroid and in the lateral direction (Fig. 5 E(ii), $F_{Rear} \approx 31\%$; $F_{side} \approx 47\%$), in agreement with force profiles of DCs reported earlier using other systems (28). However, we did not find differences in magnitudes for these migratory forces depending upon location (Fig. 5 E(iii)). Stimulation by PGE2 reduced the ability of cells to exert measurable forces (Fig. S14 B). Overall we found that iDCs migrated independently of the fiber alignment by applying forces that mostly originated laterally.

DISCUSSION

DCs are highly dynamic cells whose migratory mechanisms are an essential aspect of adaptive immune responses. Here, we developed new knowledge surrounding the role of the underlying ECM fiber architecture in controlling iDC migration paths associated with high and low motility cycles. Interestingly, we observed a subpopulation of fastmoving iDCs, for which the aligned substrates do not necessarily induce 1D-aligned migration. We hypothesize that this small portion of fast-moving iDCs is either the result of a subpopulation of iDCs that is present within the pool of differentiated cells or the result of iDCs switching between fast and slow migration modes on the suspended nanofibers. Interestingly, we have previously observed occasional switching of migration modes on 2D where a relatively nonmotile period was followed by a motile phase with enhanced protrusive activity and podosome formation at the cell edge (61).

The 2D random walks by iDCs seemed to be induced by a force-migration coupling of filamentous protrusions with fibers. We analyzed the orientation, protrusive motions, and

force distributions around the cell body and this suggested a dual function of migrating iDCs to continuously probe their environments for antigen capture at the front of the cell (24) while concentrating forces at the sides or rear of the cell to facilitate migration. We found that iDC protrusions in both 200 and 500 nm fibers, were localized at the front of the migrating directions. Our findings of a higher number of protrusions on smaller 200 nm fibers suggest a potential impact on iDC functions such as antigenic uptake (24). Although the mechanisms for the forces associated with the protrusions remain to be elucidated, they may be induced by the molecular clutch mechanism as has been described for macrophages during receptor-mediated phagocytosis (62). Future investigations to detail the localization of receptors and clutch proteins could help to better understand the origin of the forces. Interestingly, the presence of PGE2 reduced the overall protrusive activity and concentrated it to the back of the cell, impacting the migratory persistence and protrusive events in iDCs. Increasing the fiber diameter to 500 nm resulted in reduced protrusive activity, lower persistence, and less front/back polarity. These findings suggest that larger fiber diameters occasionally associated with fibrosis in aging (63), wound healing (64), and cancer (65) can potentially inhibit the overall migration ability of iDCs.

We qualitatively contrasted the impact on podosome organization and observed areas of actin enrichment on 500 nm diameter fibers that were not present on 200 nm fibers. This suggests that, when confronted with the lesser available substrate (as in our case of reduced fiber diameter), podosomes cannot be assembled properly by iDCs, something that corresponds well with the notion that an adhesive substrate is required for podosome formation (22). Furthermore, while it has been established that the number of podosomes is unaffected by the pattern of the underlying 2D geometry (22), our data suggest that the presence of a 3D nano surface such as the fibers may impact the enrichment of actin. The flux of vinculin cluster formation has been linked to the directional growth of actin filaments (61); thus, further studies could potentially capture a link between the regulation of podosome adhesions through fiber diameters and inflammation markers.

iDC cortical stiffness can be increased by the upregulation of fascin, which in turn increases the activation of RhoGTPases that regulate the expression of Arp2/3 and formins (66). In this work, we tested the role of Arp2/3 and formins as well as the response to PGE2, which is known to activate RhoA in DCs on flat substrates (7), thus impacting cell motility. We noted that the inhibition of Arp2/3 and formins critically impacted iDC migration and force generation, which matches with previous studies that noted the importance of the Arp2/3 complex iDC migration on micropost arrays (from ~13 to ~9 nN) (67). Importantly, for PGE2, we observed an overall reduction in protrusive activity but migration remained similar,

which contrasts with the increased speed of iDCs observed after PGE2 stimulation on flat surfaces (7,68). This finding is particularly interesting since this observation aligns with our observations that topographical cues can interfere with PGE2-mediated signaling in iDCs (22). Moreover, it has also been reported by others that PGE2 stimulation does not necessarily increase the migration of iDCs in 3D environments (8). Together, these results suggest that the migratory behavior in response to PGE2 is strongly influenced by the physical properties of the environment in which the DCs reside. For future studies, it would be valuable to determine the molecular mechanisms that orchestrate the interplay between topographical conditions and PGE2-mediated cytoskeletal remodeling to better understand how DCs respond to different types of ECM environments encountered in vivo.

The forces measured by our system have similar magnitudes and patterns (front, side, and back of the cell) compared with reported measurements from micropost-based force measurement systems (28,67). However, our studies extend the knowledge by showing that DC migration in aligned fibrous environments can be random as iDCs concentrate forces to their sides and back of the migrating cell body, which resembles ameboid traction force polarity (69). Our fiber platform can control individual parameters, which is difficult to control in 3D gels (70). We focused on the role of fibrillar diameters in iDC migration, where we found that the reduction increased the variability of the migrational speeds. These results would be consistent with the role of low mechanical stiffness in other systems in enhancing the speed and migratory persistence in confined agarose gels (71). However, because of the highly random orientation and arrangement of pores in 3D gel systems, it is difficult to establish direct comparisons. iDCs in other 3D gel and confinement systems exhibit dynamic pseudopods as those we recapitulate in our fibrous environments (8,72).

CONCLUSION

Overall, we report an unusual force-migration coupling in DC migration through filamentous protrusions studied on nanofibers, which propel a migratory subpopulation that we studied separately. Their protrusions concentrate at the front of the migrating cell and are clearly reoriented under PGE2 stimulus. The forces associated with cell movements have higher incidence at the rear and side of the cell, which in turn allows cells to migrate in dynamic directions not aligned with the fiber axis. We determined that these migratory capabilities on nanofibers were critically regulated by formins and myosin II. Studies addressing the molecular mechanisms driving the response of DCs and other myeloid cells to various mechanical signals from their environment are significantly increasing, testifying to the pathophysiological relevance of investigating myeloid cell mechanobiology (73). Our studies using ECM-mimicking fiber networks emphasize the need to

investigate the mechanical cues of myeloid cell dynamic protrusions on fiber networks, as they may occur in vivo during organ fibrosis or in response to implanted biomaterials.

SUPPORTING MATERIAL

Supporting material can be found online at https://doi.org/10.1016/j.bpj. 2024.07.011.

AUTHOR CONTRIBUTIONS

A.S.N., A.C., and K.v.d.D. designed the study. C.H.-P. and B.J. conducted experiments. C.H.-P., A.S.N., and K.v.d.D. analyzed the data. C.H.-P. wrote the manuscript. A.S.N., A.C., and A.F. arranged resources. All authors edited the manuscript.

ACKNOWLEDGMENTS

The authors thank members of the Spinneret-based Tunable Engineered Parameters (STEP) Lab, Virginia Tech, for helpful suggestions and discussions. The authors thank the Institute of Critical Technologies and Sciences (ICTAS) and Macromolecules Innovation Institute at Virginia Tech for their support in conducting this study. A.S.N. acknowledges partial support for this study from National Science Foundation (NSF grant nos. 2119949 and 2107332). A.S.N., A.F., and C.H.-P. acknowledge support from the National Institutes of Health (R01CA214511-04-S1). We are grateful to the Radboud Technology Center Microscopy for the use of their facilities. B.J. was supported by an NWO KLEIN grant (OCENW.KLEIN.494) awarded to K.v.d.D.

DECLARATION OF INTERESTS

The authors declare no competing interests.

REFERENCES

- 1. Dharampuriya, P. R., G. Scapin, ..., D. I. Shah. 2017. Tracking the Origin, Development, and Differentiation of Hematopoietic Stem Cells. Curr. Opin. Cell Biol. 49:108-115.
- 2. Merad, M., P. Sathe, ..., A. Mortha. 2013. The Dendritic Cell Lineage: Ontogeny and Function of Dendritic Cells and Their Subsets in the Steady State and the Inflamed Setting. *Annu. Rev. Immunol.* 31:563–604.
- 3. Puhr, S., J. Lee, ..., K. Liu. 2015. Dendritic Cell Development History, Advances, and Open Questions. Semin. Immunol. 27:388-396.
- 4. Martín-Fontecha, A., A. Lanzavecchia, and F. Sallusto. 2009. Dendritic cell migration to peripheral lymph nodes. Handb. Exp. Pharmacol. 188:31-49.
- 5. Chizzolini, C., and N. Costantino Brembilla. 2009. Prostaglandin E2: igniting the fire. Immunol. Cell Biol. 87:510-511.
- 6. Harizi, H., and N. Gualde. 2006. Pivotal Role of PGE 2 and IL-10 in the Cross-Regulation of Dendritic Cell-Derived Inflammatory Mediators. Cell. Mol. Immunol. 3:271-277.
- 7. van Helden, S. F. G., M. M. Oud, ..., F. N. van Leeuwen. 2008. PGE2mediated podosome loss in dendritic cells is dependent on actomyosin contraction downstream of the RhoA-Rho-kinase axis. J. Cell Sci. 121:1096-1106.
- 8. Cougoule, C., C. Lastrucci, ..., I. Maridonneau-Parini. 2018. Podosomes, But Not the Maturation Status, Determine the Protease-Dependent 3D Migration in Human Dendritic Cells. Front. Immunol. 9:846.

- Lee, A. W., T. Truong, ..., N. Bhardwaj. 2002. A clinical grade cocktail
 of cytokines and PGE2 results in uniform maturation of human monocyte-derived dendritic cells: implications for immunotherapy. *Vaccine*.
 20:A8–A22.
- Bonasio, R., and U. H. von Andrian. 2006. Generation, migration and function of circulating dendritic cells. Curr. Opin. Immunol. 18:503–511.
- Worbs, T., S. I. Hammerschmidt, and R. Förster. 2017. Dendritic cell migration in health and disease. *Nat. Rev. Immunol.* 17:30–48.
- Alvarez, D., E. H. Vollmann, and U. H. von Andrian. 2008. Mechanisms and Consequences of Dendritic Cell Migration. *Immunity*. 29:325–342.
- Flores-Romo, L. 2001. In vivo maturation and migration of dendritic cells. *Immunology*. 102:255–262.
- Renkawitz, J., K. Schumann, ..., M. Sixt. 2009. Adaptive force transmission in amoeboid cell migration. *Nat. Cell Biol.* 11:1438–1443.
- Huttenlocher, A., and A. R. Horwitz. 2011. Integrins in cell migration. Cold Spring Harbor Perspect. Biol. 3:a005074.
- Wang, S., Y. Chen, ..., Q. Chen. 2022. The role of dendritic cells in the immunomodulation to implanted biomaterials. *Int. J. Oral Sci.* 14:52.
- Zhang, B., Y. Su, ..., D. Zhu. 2021. Toward a Better Regeneration through Implant-Mediated Immunomodulation: Harnessing the Immune Responses. Adv. Sci. 8:e2100446.
- Sanders, J. E., C. E. Stiles, and C. L. Hayes. 2000. Tissue response to single-polymer fibers of varying diameters: Evaluation of fibrous encapsulation and macrophage density. J. Biomed. Mater. Res. 52:231–237.
- Ward, W. K., E. P. Slobodzian, ..., M. D. Wood. 2002. The effect of microgeometry, implant thickness and polyurethane chemistry on the foreign body response to subcutaneous implants. *Biomaterials*. 23:4185–4192.
- Gammon, J. M., and C. M. Jewell. 2019. Engineering Immune Tolerance with Biomaterials. Adv. Healthcare Mater. 8:1801419.
- Gunzer, M., P. Friedl, ..., K. S. Zanker. 2000. Migration of dendritic cells within 3-D collagen lattices is dependent on tissue origin, state of maturation, and matrix structure and is maintained by proinflammatory cytokines. *J. Leukoc. Biol.* 67:622–629.
- Van Den Dries, K., S. F. G. Van Helden, ..., C. G. Figdor. 2012. Geometry sensing by dendritic cells dictates spatial organization and PGE 2-induced dissolution of podosomes. *Cell Mol. Life Sci.* 69:1889–1901.
- Vargas, P., M. Chabaud, ..., A. M. Lennon-Dumenil. 2016. Study of dendritic cell migration using micro-fabrication. *J. Immunol. Methods*. 432:30–34.
- Chabaud, M., M. L. Heuze, ..., A. M. Lennon-Dumenil. 2015. Cell migration and antigen capture are antagonistic processes coupled by myosin II in dendritic cells. *Nat. Commun.* 6:1–16.
- Faure-André, G., P. Vargas, ..., A. M. Lennon-Duménil. 2008. Regulation of dendritic cell migration by CD74, the MHC class II-associated invariant chain. Science. 322:1705–1710.
- Mennens, S. F. B., K. van den Dries, and A. Cambi. 2017. Role for mechanotransduction in macrophage and dendritic cell immunobiology. *Results Probl. Cell Differ.* 62:209–242.
- Vesperini, D., G. Montalvo, ..., F. Lautenschläger. 2021. Characterization of immune cell migration using microfabrication. *Biophys. Rev.* 13:185–202.
- Ricart, B. G., M. T. Yang, ..., D. A. Hammer. 2011. Measuring traction forces of motile dendritic cells on micropost arrays. *Biophys. J.* 101:2620–2628.
- Wu, P. H., A. Giri, ..., D. Wirtz. 2014. Three-dimensional cell migration does not follow a random walk. *Proc. Natl. Acad. Sci. USA*. 111:3949–3954.
- Yamada, K. M., and M. Sixt. 2019. Mechanisms of 3D cell migration. Nat. Rev. Mol. Cell Biol. 20:738–752.
- 31. Petrie, R. J., and K. M. Yamada. 2016. Multiple mechanisms of 3D migration: the origins of plasticity. *Curr. Opin. Cell Biol.* 42:7–12.
- 32. Petrie, R. J., and K. M. Yamada. 2012. At the leading edge of three-dimensional cell migration. *J. Cell Sci.* 125:5917–5926.

- Petrie, R. J., N. Gavara, ..., K. M. Yamada. 2012. Nonpolarized signaling reveals two distinct modes of 3D cell migration. *J. Chromatogr. B*. 197:439–455.
- Wang, J., and A. S. Nain. 2014. Suspended micro/nanofiber hierarchical biological scaffolds fabricated using non-electrospinning STEP technique. *Langmuir*. 30:13641–13649.
- Nain, A. S., M. Sitti, ..., C. Amon. 2009. Dry spinning based spinneret based tunable engineered parameters (STEP) technique for controlled and aligned deposition of polymeric nanofibers. *Macromol. Rapid Commun.* 30:1406–1412.
- Meehan, S., and A. S. Nain. 2014. Role of Suspended Fiber Structural Stiffness and Curvature on Single-Cell Migration, Nucleus Shape, and Focal-Adhesion-Cluster Length. *Biophys. J.* 107:2604–2611.
- Mukherjee, A., J. E. Ron, ..., A. S. Nain. 2023. Actin Filaments Couple the Protrusive Tips to the Nucleus through the I-BAR Domain Protein IRSp53 during the Migration of Cells on 1D Fibers. Adv. Sci. 10:2207368.
- Padhi, A., B. E. Danielsson, ..., A. S. Nain. 2021. Cell Fragment Formation, Migration, and Force Exertion on Extracellular Mimicking Fiber Nanonets. Adv. Biol. 5:2000592.
- Padhi, A., A. H. Thomson, ..., D. A. Brown. 2020. Bioenergetics underlying single-cell migration on aligned nanofiber scaffolds. *Am. J. Physiol. Cell Physiol.* 318:C476–C485.
- Graybill, P. M., A. Jana, ..., R. V. Davalos. 2021. Single Cell Forces after Electroporation. ACS Nano. 15:2554–2568.
- Jana, A., A. Tran, ..., T. Kevin. 2022. Sculpting Rupture-Free Nuclear Shapes in Fibrous Environments. Adv. Sci. 9:2203011.
- Sheets, K., J. Wang, ..., A. S. Nain. 2016. Nanonet Force Microscopy for Measuring Cell Forces. *Biophys. J.* 111:197–207.
- Nain, A. S., and J. Wang. 2013. Polymeric nanofibers: isodiametric design space and methodology for depositing aligned nanofiber arrays in single and multiple layers. *Polym. J.* 45:695–700.
- Siadat, S. M., A. A. Silverman, ..., J. W. Ruberti. 2021. Measuring collagen fibril diameter with differential interference contrast microscopy. J. Struct. Biol. 213:107697.
- **45.** Thurner, B., C. Röder, ..., G. Schuler. 1999. Generation of large numbers of fully mature and stable dendritic cells from leukapheresis products for clinical application. *J. Immunol. Methods.* 223:1–15.
- de Vries, I. J. M., G. J. Adema, ..., C. G. Figdor. 2002. Phenotypical and functional characterization of clinical-grade dendritic cells. J. Immunother. 25:429–438.
- Hall, A., P. Chan, ..., A. Nain. 2017. Nanonet force microscopy for measuring forces in single smooth muscle cells of the human aorta. *Mol. Biol. Cell.* 28:1894–1900.
- Padhi, A., K. Singh, ..., A. S. Nain. 2020. Force-exerting perpendicular lateral protrusions in fibroblastic cell contraction. *Commun. Biol.* 3:390.
- Sheets, K., S. Wunsch, ..., A. S. Nain. 2013. Shape-dependent cell migration and focal adhesion organization on suspended and aligned nanofiber scaffolds. *Acta Biomater*. 9:7169–7177.
- Singh, J., A. Pagulayan, and A. Nain. 2020. Rules of Contact Inhibition of Locomotion in Cells Migrating on ECM Mimicking Fibers. *Proc. Natl. Acad. Sci. USA*. 118:e2011815118.
- Elina, M., L. Heuz, ..., A.-M. Lennon-Duménil. 2013. Migration of dendritic cells: physical principles, molecular mechanisms, and functional implications. *Immunol. Rev.* 256:240–254.
- 52. Jana, A., I. Nookaew, ..., A. S. Nain. 2019. Crosshatch nanofiber networks of tunable interfiber spacing induce plasticity in cell migration and cytoskeletal response. *FASEB J.* 33:10618–10632.
- Estabridis, H. M., A. Jana, ..., D. J. Odde. 2018. Cell Migration in 1D and 2D Nanofiber Microenvironments. *Ann. Biomed. Eng.* 46:392–403.
- Pollard, T. D., and G. G. Borisy. 2003. Cellular Motility Driven by Assembly and Disassembly of Actin Filaments. Cell. 112:453–465.
- Vargas, P., P. Maiuri, ..., A. M. Lennon-Duménil. 2016. Innate control of actin nucleation determines two distinct migration behaviours in dendritic cells. *Nat. Cell Biol.* 18:43–53.

- 56. Lämmermann, T., and M. Sixt. 2009. Mechanical modes of 'amoeboid' cell migration. Curr. Opin. Cell Biol. 21:636-644.
- 57. Lämmermann, T., B. L. Bader, ..., M. Sixt. 2008. Rapid leukocyte migration by integrin-independent flowing and squeezing. Nature. 453:51-55.
- 58. Lauffenburger, D. A., and A. F. Horwitz. 1996. Cell migration: A physically integrated molecular process. Cell. 84:359-369.
- 59. Kang, J. H., H. J. Lee, ..., H. J. Lee. 2021. Biomechanical forces enhance directed migration and activation of bone marrow-derived dendritic cells. Sci. Rep. 11:12106.
- 60. de Winde, C. M., C. Munday, and S. E. Acton. 2020. Molecular mechanisms of dendritic cell migration in immunity and cancer. Med. Microbiol. Immunol. 209:515-529.
- 61. Meddens, M. B. M., E. Pandzic, A. Cambi..., 2016. Actomyosindependent dynamic spatial patterns of cytoskeletal components drive mesoscale podosome organization. Nat. Commun. 7:13127.
- 62. Jaumouillé, V., A. X. Cartagena-Rivera, and C. M. Waterman. 2019. Coupling of \(\beta \) integrins to actin by a mechanosensitive molecular clutch drives complement receptor-mediated phagocytosis. Nat. Cell Biol. 21:1357-1369.
- 63. Lee, S., M. N. Islam, ..., M. Bhattacharya. 2021. Molecular programs of fibrotic change in aging human lung. Nat. Commun. 12:6309-6310.
- 64. Diegelmann, R. F., and M. C. Evans. 2004. Wound healing: An overview of acute, fibrotic and delayed healing. Front. Biosci. 9:283-289.

- 65. Chandler, C., T. Liu, ..., L. G. Coffman. 2019. The double edge sword of fibrosis in cancer. Transl. Res. 209:55-67.
- 66. Blumenthal, D., V. Chandra, ..., J. K. Burkhardt. 2020. Mouse t cell priming is enhanced by maturation-dependent stiffening of the dendritic cell cortex. Elife. 9:1-44.
- 67. Bendell, A. C., E. K. Williamson, ..., D. A. Hammer. 2017. The Arp2/3 complex binding protein HS1 is required for efficient dendritic cell random migration and force generation. Integr. Biol. 9:695-708.
- 68. van Helden, S. F. G., D. J. E. B. Krooshoop, ..., F. N. van Leeuwen. 2006. A critical role for prostaglandin E2 in podosome dissolution and induction of high-speed migration during dendritic cell maturation. J. Immunol. 177:1567-1574.
- 69. Alvarez-Gonzalez, B., E. Bastounis, ..., J. C. Lasheras. 2014. Cytoskeletal Mechanics Regulating Amoeboid Cell Locomotion. Appl. Mech.
- 70. Yang, C., C. Gao, ..., K. Dai. 2011. Preparation and characterization of three-dimensional nanostructured macroporous bacterial cellulose/ agarose scaffold for tissue engineering. J. Porous Mater. 18:545-552.
- 71. Choi, Y., J. E. Kwon, and Y. K. Cho. 2021. Dendritic Cell Migration Is Tuned by Mechanical Stiffness of the Confining Space. Cells. 10:3362.
- 72. Barbier, L., P. J. Sáez, ..., P. Vargas. 2019. Myosin II activity is selectively needed for migration in highly confined microenvironments in mature dendritic cells. Front. Immunol. 10:436547.
- 73. Janssen, E., K. van den Dries, ..., A. Cambi. 2024. Mechanobiology of myeloid cells. Curr. Opin. Cell Biol. 86:102311.